Chapter 6
Artificial refraction of radiowaves in the ionosphere

§ 1. Introduction

In this chapter, we will consider the dispersion refraction effect based on the principle of monochromatic wave superposition, using the practical application of this principle – artificial control of radio propagation in the ionosphere – as an example.

To form required frequency modulation, we will use transformation of longitudinal wave packet modulation into transverse modulation due to the inhomogeneous structure of the ionosphere. Although this method largely depends on the inhomogeneous structure of a medium, the method has one significant advantage: the possibility of using ordinary antennas instead of bulky antenna arrays.

Several considerations explain why we use the superposition principle.

First, a number of wel-known approximate methods are used to solve monochromatic problems for complex media close to real ones. We will use the parabolic wave equation in the diffraction theory.

Second, the inverse problem of synthesizing an emitted signal, which maintains a maximal energy at a specified spatial point when propagating in the ionosphere, becomes simple and is reduced to the selection of phases and amplitudes of monochromatic components.

Third, we have the methodological objective: to consider dispersion refraction from different viewpoints.

First of all, we state that the superposition principle is valid for wave function U because this function satisfies the linear wave equation (1.7). At the same time, this principle is invalid for the wave energy characteristics, e.g., for power and energy, because these characteristics are nonlinear functions of the field.

However, precisely energy characteristics are of practical interest. For example, in the most common applied problem of radiophysics – messaging with the help of radiowaves – reception reliability depends on

a signal energy. Moreover, the conception of radio propagation is related to wave energy propagation. For example, group velocity in STRO is an average energy transfer rate during a period.

Within the scope of the spectral approach, dispersion refraction is explained by the effect of frequency-dependent focusing, similar to compression of a longitudinally modulated wave during time dispersion in the one-dimensional case [32, 33, 51, 52, 61, 68]. A packet will have the maximal power at a spatial point and instant when the phases of all spectral components coincide.

In the one-dimensional case, only power can be redistributed in space, and the total packet energy remains unchanged at any spatial point. Naturally, the dispersion refraction effect cannot be observed here by definition.

In two- and three-dimensional cases, energy can be redistributed in space, if monochromatic components have differently directed wavevectors, as is observed in a wave packet with transverse frequency modulation. In such a case, transverse focusing will originate in addition to longitudinal focusing, and energy will be redistributed in space as a result of a joint action of this focusing. The total energy in the entire spatial region will certainly remain unchanged.

This redistribution is physically explained by the appearance of the dispersion refraction effect and can be described within the scope of STRO (see below).

On the global scales, the ionosphere, where the strongest dispersion is observed in the HF band of radiowaves, is the most extensive dispersing medium. As was mentioned above, dispersion effects appear here at a bandwidth of 100 kHz [34, 48, 53, 57, 97]. Note, that almost all HF radio systems have narrower bands because developers of such systems try to avoid dispersive signal distortions in a radio channel. This mainly explains why the dispersion refraction effect is not observed in ordinary narrowband systems: since this phenomenon is a multi-dimensional version of wave packet dispersive distortions.

Several recent works [109, 110] studied the possibility of compensating longitudinal dispersive distortion of an ionospheric radiosignal using special filters in order to process this signal, which makes it possible to expand the radio channel band up to 1 MHz.

The effect of field amplification at a certain spatial point due to dispersion of a medium based on the superposition principle is illustrated by Fig. 17. Assume that a transmitter emits a signal with a sufficiently broad frequency spectrum in a rather wide range of angles, and the plasma frequency of the ionosphere monotonically increases with altitude.

Different frequency components of the signal spectrum will evidently come to a receiving point at different angles since they will be re-

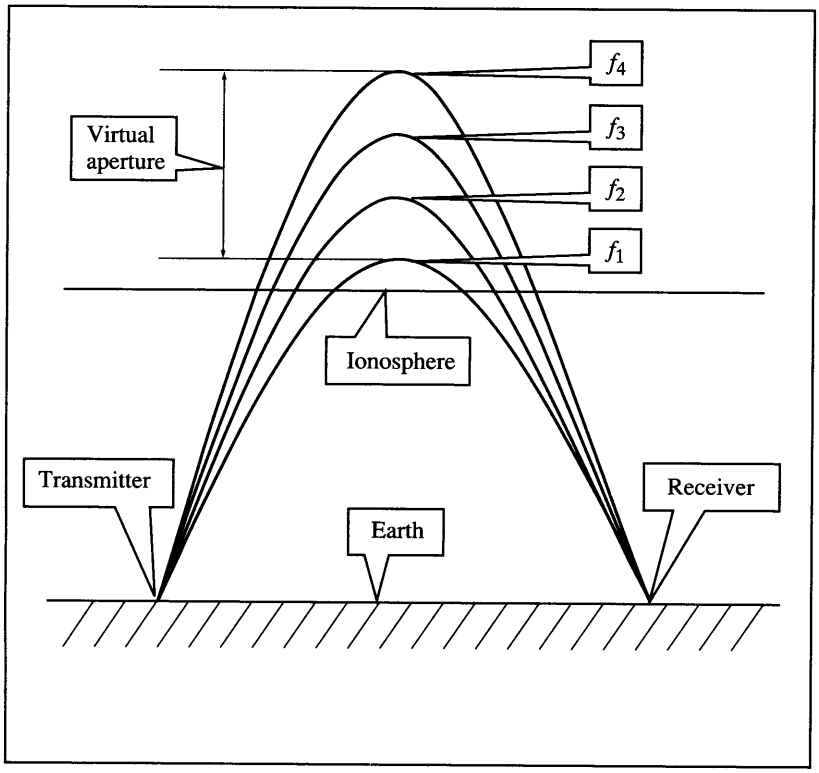

Fig. 17. Scheme of field focusing at a chosen point in a nonuniform dispersive medium

flected at different ionospheric altitudes due to dispersion. If phases of all frequency components coincide at a receiving point, packet compression in time will be accompanied by packet compression in space, including transverse direction.

The origination of a large-aperture virtual antenna, focusing wave energy in the ionosphere, can also explain field amplification at a receiving point.

The possibility of adaptively focusing HF signals in the ionospheric radio channel was referred to previously, but dispersion properties of the ionosphere were not used [107]. The fundamental feature of our approach is to reject bulky phased antenna arrays.

The main goal of this chapter is to show that time dispersion of a medium can be used to create artificial refraction with practically significant magnitude.

For this purpose, we will numerically compute propagation of several monochromatic signal components in a simplified model of the iono-

sphere with one linear layer and will sum the components with identical phases at a selected spatial point. The condition of phasing monochromatic components at a selected point is easily converted to their initial phases at an emission point, which makes it possible to calculate (synthesize) an emitted pulse.

Using the inverse Fourier transform, we will determine the spatial-temporal packet characteristics and will calculate the energy distribution in the spatial-temporal coordinates.

Then, using the longitudinal frequency modulation parameters of a synthesized emitted packet, we will calculate the trajectories of the space – time ray with the help of the formulas of modified STRO and will compare the results with the wave calculations.

§ 2. Problem statement

Let us consider wave packet propagation in a rectangular domain $[0, L_x]$, $[0, L_y]$ along the x and y axes, simulating a section of the ionospheric radio channel. Here the x axis corresponds to the longitudinal coordinate, along which radiowaves mainly propagate, and the y axis corresponds to altitude. Figure 18 shows the vertical distribution of a plasma electron frequency, which is the simplest model of the ionosphere with a single linear layer [34]. Assume that signal $A_p(t)$ with the spectrum

$$A_s(\omega) = \frac{1}{2\pi} \int_{-\infty}^{\infty} A_p(t) \exp(i\omega t)\, dt$$

is emitted from point $x = 0$, $y = 0$ on the Earth's surface.

For each spectral component of a signal, we solve the problem of monochromatic wave propagation in a parabolic approximation. This approximation can be used because only waves with small elevation angles participate in long-range HF propagation.

Recall that a parabolic (or small-angle) approximation is obtained by substituting the Ansatz

$$U = A \exp\left\{ i\left(\frac{\omega}{c} x - \omega t \right) \right\}$$

into the initial wave equation (1.7) and by rejecting the $\partial^2 A/\partial x^2$ term.

The parabolic equation of the diffraction theory has the following form [37, 64, 98, 99]:

$$\frac{\partial^2 A}{\partial y^2} - 2i \frac{\omega}{c} \frac{\partial A}{\partial x} - \frac{\omega_L^2}{c^2} A = 0. \qquad (6.1)$$

Here $A(x, y)$ is the complex-valued field amplitude dependent on the spatial coordinates x and y.

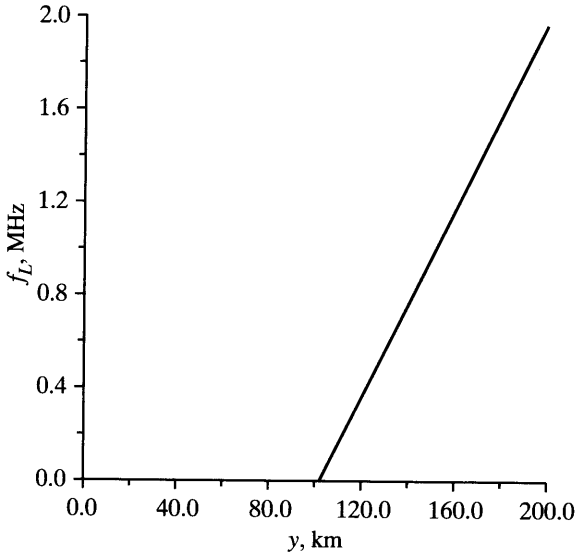

Fig. 18. Vertical prifile of the electron plasma frequency

Equation (6.1) gives a minute error as compared to the initial wave equation (1.7), if the following condition is satisfied in the computational domain:

$$\frac{\omega}{c}\frac{\partial A}{\partial x} \gg \frac{\partial^2 A}{\partial x^2}. \tag{6.2}$$

This condition physically means that a wave propagates at small angles with respect to the x axis. In this case A is a slow function of spatial coordinates, which makes it possible to effectively use numerical methods to solve the parabolic equation (6.1).

We computed each spectral component, beginning from distance x_0, where we specified the initial conditions $A(y)$ corresponding to the Gaussian beam radiated from point $x = 0, y = 0$. At all frequencies, the initial field has the identical spatial envelope curves and zero initial phase.

A change in the boundary amplitude or phase of function $A(y)$ will evidently result in the same change in the amplitude and phase at all spatial points. The inverse statement is also true: if we want to change the phase and amplitude at any spatial point, we should identically change the initial field parameters. Below we will use these statements in order to synthesize a radiated signal.

The specific aim of this chapter is to show (by means of computations) that focusing of the spectral components in the space and time domain multiply increases wave packet energy as compared to the monochromatic case.

To focus field energy at a selected point x_m, y_m, it is necessary to equalize the phases of all spectral components at this point. At each frequency ω for all altitudes y, this procedure is expressed by the formula

$$\tilde{A}(x_m, y, \omega) = \frac{A(x_m, y, \omega)}{A(x_m, y_m, \omega)} |A(x_m, y_m, \omega)|.$$

Moreover, to improve the field distribution characteristics, during summation we should use weighting coefficients $\varkappa(|A|)$ depending on the amplitude absolute value. After the equalization of phases and the weighting procedure, the two-dimensional wave packet function $A_\omega(y, t)$ at distance x_m focused at height y_m is expressed in terms of the inverse Fourier transform:

$$A_\omega(y, t) = \int_{-\infty}^{\infty} \frac{A(x_m, y, \omega)}{A(x_m, y_m, \omega)} |A(x_m, y_m, \omega) \times$$

$$\times |A(x_m, y_m, \omega)| \varkappa |A(x_m, y_m, \omega)| \exp(-i\omega t) d\omega.$$

The emitted pulse wave form is also expressed in terms of the inverse Fourier transform:

$$A_p(t) = \int_{-\infty}^{\infty} \frac{A^*(x_m, y_m, \omega)}{|A(x_m, y_m, \omega)|} \varkappa(|A(x_m, y_m, \omega)|) \exp(-i\omega t) d\omega.$$

As usual, an asterisk means complex conjugation.

§ 3. Results of numerical computations using the parabolic equation

The implicit, unconditionally stable, finite-difference Crank–Nicholson scheme of the second order of accuracy [15] was used to numerically solve the parabolic equation (6.1).

Initial vertical field distribution at a distance of $x_0 = 300$ km for every of 100 frequencies in the frequency band 4.75–5.25 MHz was specified in the form of a Gaussian beam, centered at $y_0 = 45$ km, with a half – width of $\sigma = 9{,}5$ km and a phase front curvature radius of $R = 340$ km:

$$A(y) = \exp\left\{-\frac{(y - y_0)^2}{\sigma^2} - ik(y - y_0)\sin\alpha - ik\frac{(y - y_0)^2}{R}\right\}.$$

Here $\alpha = 0.175$ is the beam elevation angle.

Figures 19–22 show the vertical field distribution for a central frequency of 5 MHz at distances of $x = 300$, 650, 1300, and 1700 km. These figures can be used to trace all beam propagation stages and the waveform evolution. For example, Fig. 21 demonstrates beam compression in the caustic region; Fig. 22 – field amplitude distribution at a final distance of $x_m = 1700$ km.

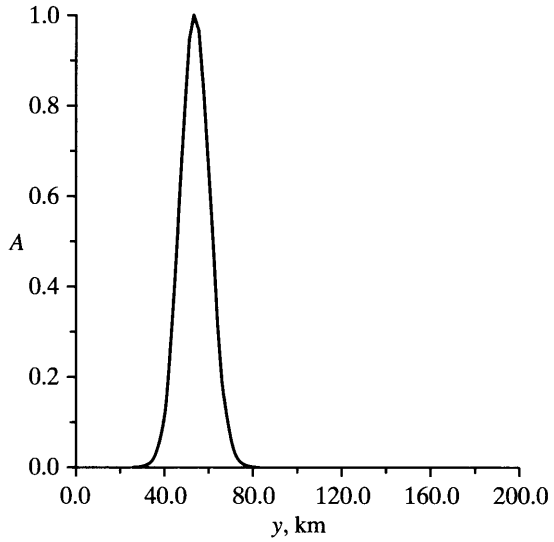

Fig. 19. Initial wave beam at $x_0 = 300$ km, $f = 5$ MHz

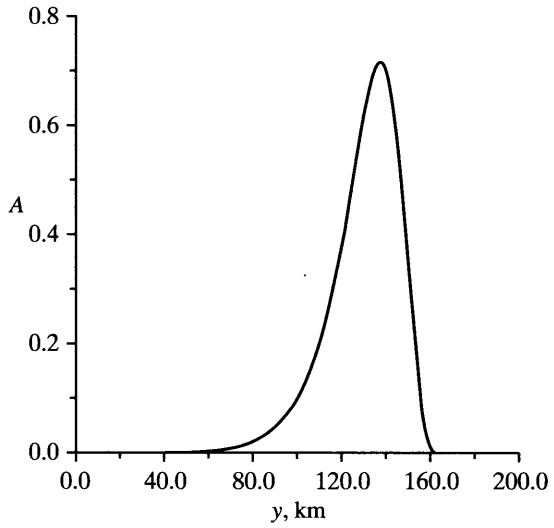

Fig. 20. Vertical field distribution at $x = 600$ km, $f = 5$ MHz

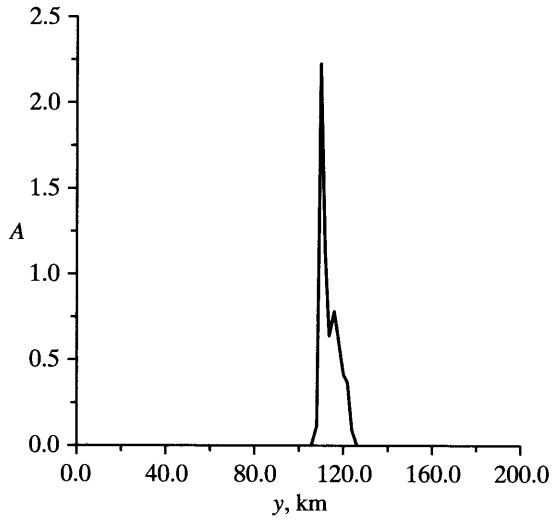

Fig. 21. Vertical field distribution at x = 1300 km, f = 5 MHz

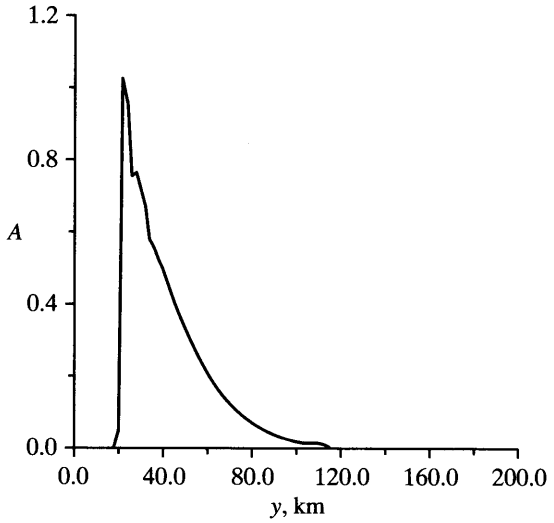

Fig. 22. Vertical field distribution at x_m = 1700 km, f = 5 MHz

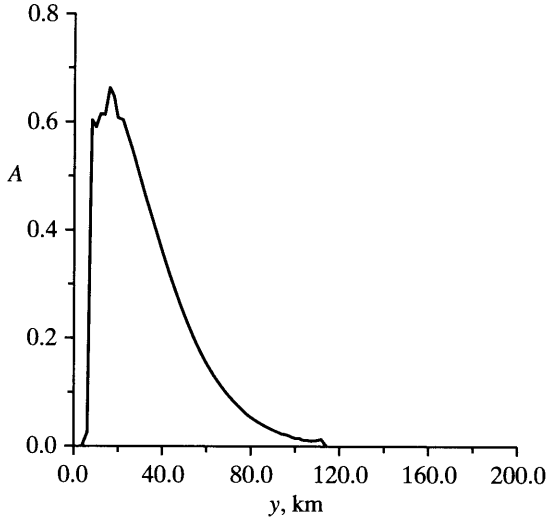

Fig. 23. Vertical field distribution at x_m = 1700 km, f = 4.75 MHz

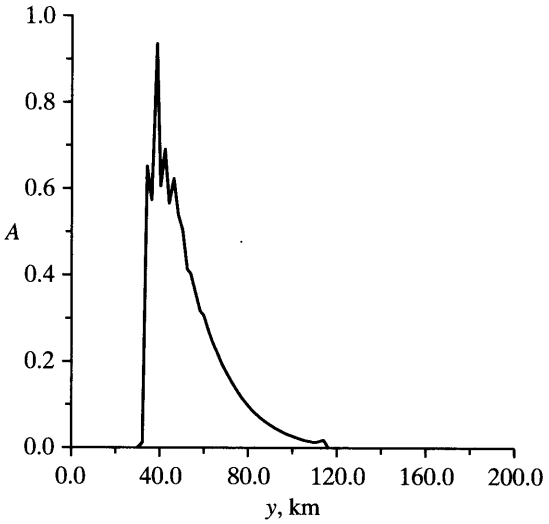

Fig. 24. Vertical field distribution at x_m = 1700 km, f = 5.25 MHz

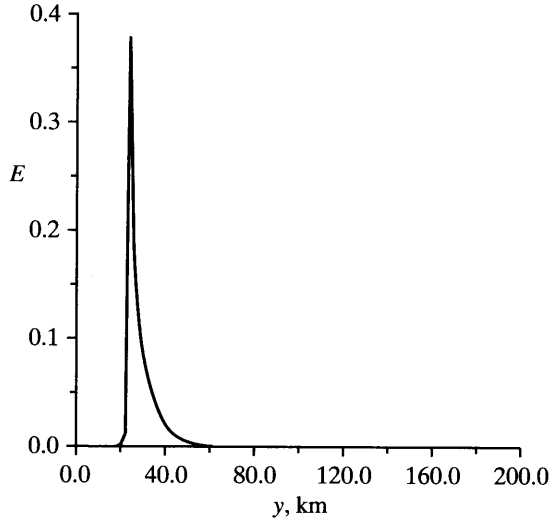

Fig. 25. Energy distribution of the wave packet focused at an altitude of $y_m = 22$ km

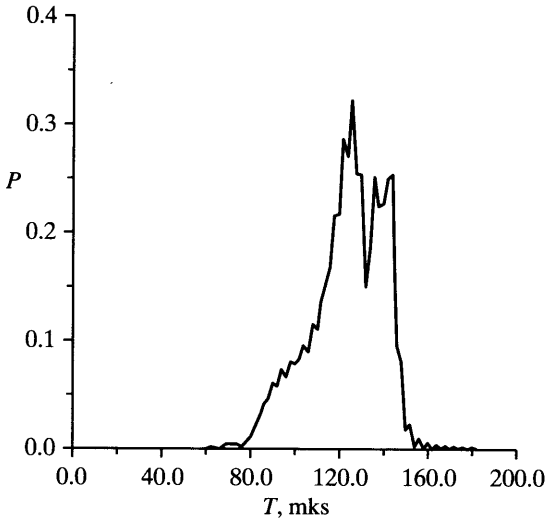

Fig. 26. Time variations in the emitted signal power providing packet focusing at an altitude of $y_m = 22$ km

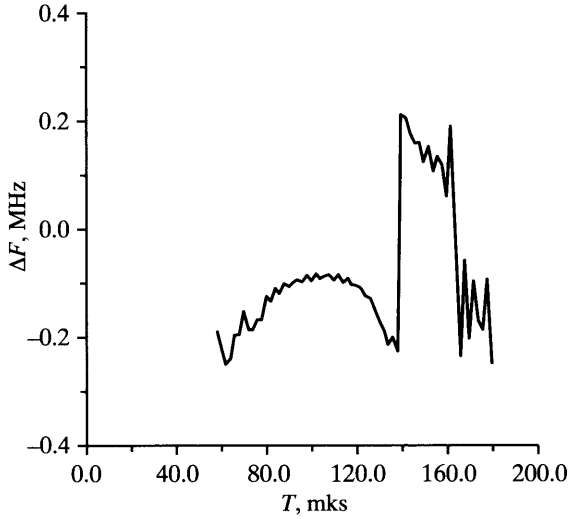

Fig. 27. Time variations in the emitted signal frequency providing the packet focusing at an altitude of y_m = 22 km

Figures 23 and 24 show the field distribution at a distance of x_m = 1700 km for two extreme frequencies of 4.75 and 5.25 MHz.

Figures 25–27 and the 3*D* plot of Fig. 31 show different characteristics of a wave packet focused at an altitude of y_m = 22 km. Hereafter, we use weighting coefficients $\varkappa = |A|^3$.

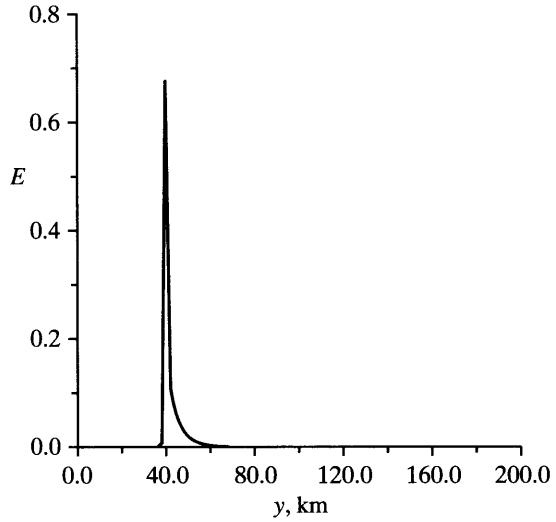

Fig. 28. Energy distribution of the wave packet focused at an altitude of y_m = 38 km

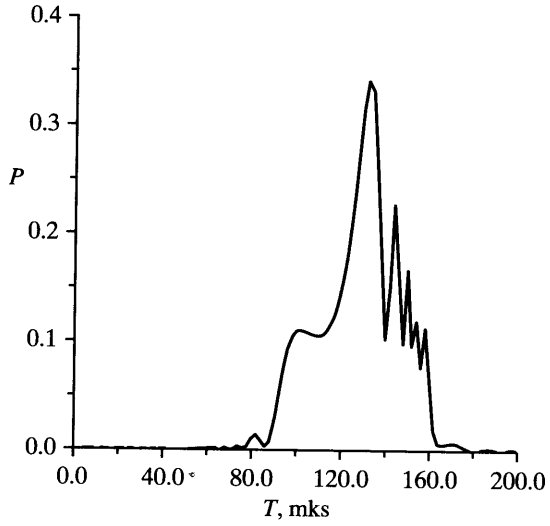

Fig. 29. Time variations in the emitted signal power providing packet focusing at an amplitude of $y_m = 38$ km

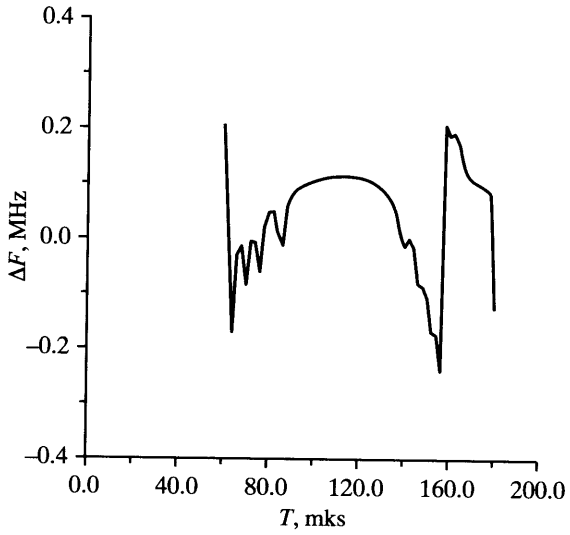

Fig. 30. Time variations in the emitted signal frequency providing packet focusing at an altitude of $y_m = 38$ km

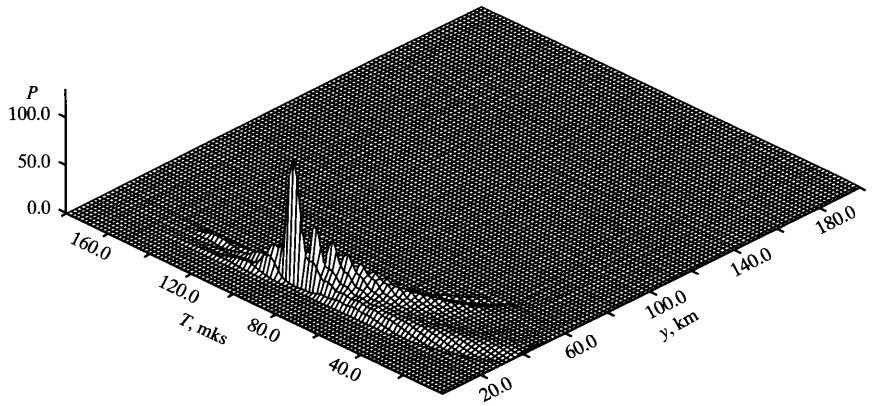

Fig. 31. Space-time power distribution of a wave packet focused at an altitude of $y_m = 22$ km

Figure 25 displays the total wave packet energy $E(y)$ as a function of altitude. The values of this energy are defined as

$$E(y) = \int_0^T W(y,t)\,dt,$$

where T is the packet duration.

It is evident that the packet energy is distinctly concentrated at an altitude of $y_m = 22$ km.

The next two plots (Fig. 26, 27) show the amplitude and frequency modulation of a synthesized emitted pulse, which is responsible for energy focusing at an altitude of 22 km.

Figure 31 displays the wave packet power distribution in the y, t coordinates. It is clear that the packet is compressed along the space and time coordinates.

Here we determined the power distribution by taking the integral over the fast oscillation period τ:

$$P(y,t) = \frac{1}{\tau}\int_{-\tau/2}^{\tau/2} W(y,\tau-\theta)\,d\theta.$$

Figures 28–30 and the 3*D* plot of Fig. 32 depict the same field characteristics, but the packet energy is focused at an altitude of $y_m = 38$ km in this case.

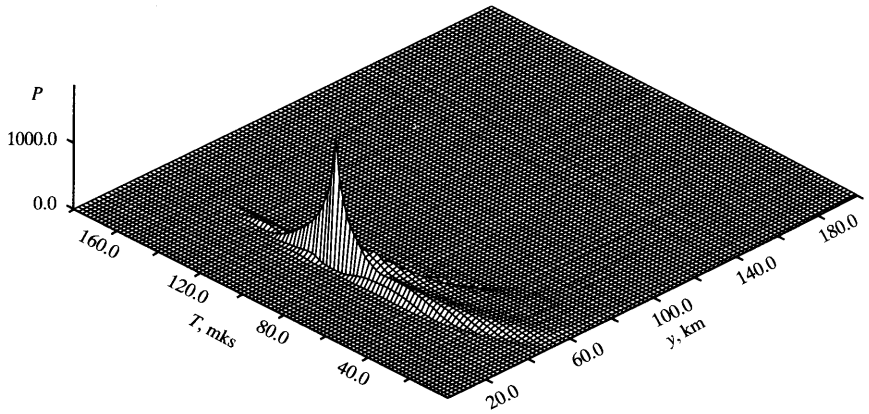

Fig. 32. Space-time power distribution of a wave packet focused at an altitude of $y_m = 38$ km

The computation results indicate that the field focusing at a given point increases the wave packet energy density by an order of magnitude as compared to this value for any monochromatic component inside the signal spectrum (on the assumption of equal emitted energies) because of a transverse energy redistribution (as was mentioned, the total energy remains unchanged along the entire altitude y).

§ 4. Results of numerical computations based on ray equations

In this section, we will present the results of the numerical space-time ray tracing, based on modified STRO, for KGE (1.7):

$$\frac{d\mathbf{r}}{dt} = \mathbf{V}_g; \tag{6.3}$$

$$\mathbf{V}_g = c^2 \frac{\mathbf{k}}{\omega}; \tag{6.4}$$

$$\frac{d\omega}{dt} = 0; \tag{6.5}$$

$$\frac{d\mathbf{V}_g}{dt} = -\frac{c^2\omega_L}{\omega^2}\nabla\omega_L + \frac{c^2\omega_L^3}{\omega^4}\nabla_\perp\omega_L - \frac{c^2\omega_L^2}{\omega^3}\nabla_\perp\omega; \tag{6.6}$$

$$\frac{dA}{dt} = -\frac{A_0}{2}\left[\frac{c^2}{\omega}D - \left(\frac{1}{k_x} - \frac{c^2 k_x}{\omega^2}\right)\Omega_x - \frac{\omega_L}{\omega k_x}\frac{\partial \omega_L}{\partial x}\right]; \tag{6.7}$$

$$\frac{dD}{dt} = -\frac{c^2}{\omega}\left(\frac{\omega_L}{c^2 k_x}\frac{\partial \omega_L}{\partial y}\right)^2 - \frac{\omega_L}{\omega}\frac{\partial^2 \omega_L}{\partial y^2} -$$

$$-\frac{\omega_L^2}{\omega(\omega^2 - \omega_L^2)}\Omega_y^2 - \frac{2\omega_L}{\omega^2 - \omega_L^2}\frac{\partial \omega_L}{\partial y}\Omega_y - \frac{c^2}{\omega}D^2; \tag{6.8}$$

$$\frac{d\Omega_x}{dt} = \frac{1}{k_x}\Omega_y^2 + \left(\frac{1}{k_x} - \frac{c^2 k_x}{\omega^2}\right)\Omega_x^2 + \frac{\omega_L}{\omega k_x}\frac{\partial \omega_L}{\partial x}\Omega_x + \frac{\omega_L}{\omega k_x}\frac{\partial \omega_L}{\partial y}\Omega_y; \tag{6.9}$$

$$\frac{d\Omega_y}{dt} = \frac{\omega_L}{\omega k_x}\frac{\partial \omega_L}{\partial x}\Omega_x - \frac{c^2}{\omega}\Omega_y D + \left(\frac{1}{k_x} - \frac{c^2 k_x}{\omega^2}\right)\Omega_x \Omega_y. \tag{6.10}$$

Here we used the following designations:

$$D = \frac{\partial k_y}{\partial y}; \quad \Omega_x = -\frac{\partial \omega}{\partial x}; \quad \Omega_y = -\frac{\partial \omega}{\partial y},$$

where D is ray divergence, Ω_x is the longitudinal frequency modulation index, and Ω_y is the transverse frequency modulation index.

Initially we obtained Eqs. (6.3)–(6.6) for KGE in Chapter 4. They are contained as a particular case in the equations for an arbitrary dispersion law, considered in Chapter 5. To pass from the general equations (5.21), (5.24a), and (5.25a) to particular equations (6.3)–(6.9), we accepted that $\varepsilon_0 = 1$, $\omega_M = \omega_L^2$.

In Eq. (6.10), the term

$$\frac{\omega_L}{\omega k_x}\frac{\partial \omega_L}{\partial y}\Omega_x$$

describes the transformation of longitudinal modulation Ω_x into transverse modulation Ω_y in an inhomogeneous transverse structure of a medium.

The above equations specify monochromatic rays without modulation, if the indices of longitudinal and transverse frequency modulation are taken equal to zero. Figure 33 displays the projections of the space-time ray trajectories onto the spatial coordinates for a monochromatic wave with a frequency of 5 MHz, which can be compared with the computations performed using the parabolic equation. Here we can trace the complete coincidence of the ray trajectories with the spatial field

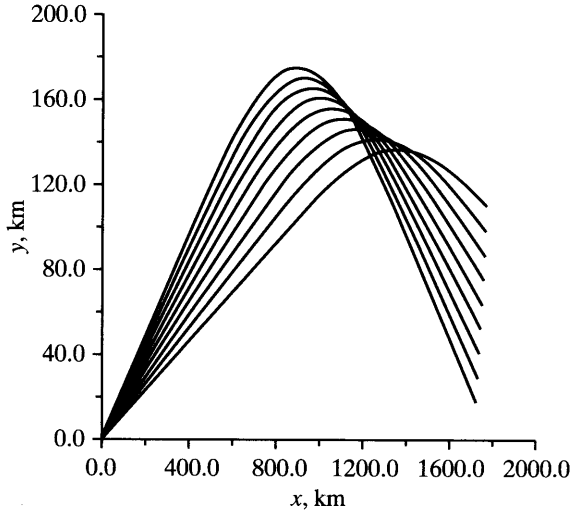

Fig. 33. Projections of space-time rays of a non-modulated wave with a frequency of $f = 5$ MHz on the spatial coordinates

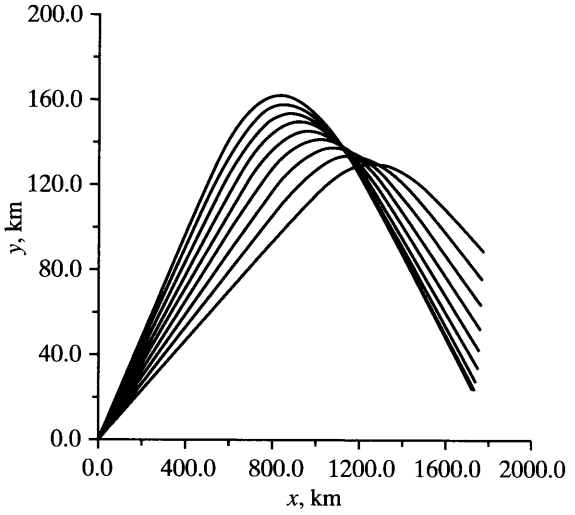

Fig. 34. Projections of space-time rays on the spatial coordinates for an instant frequency of $f = 4.89$ MHz and a longitudinal frequency modulation coefficient of $\Omega_x = 0.21$ rad / (mks · km). The packet is focused at an altitude of $y_m = 22$ km

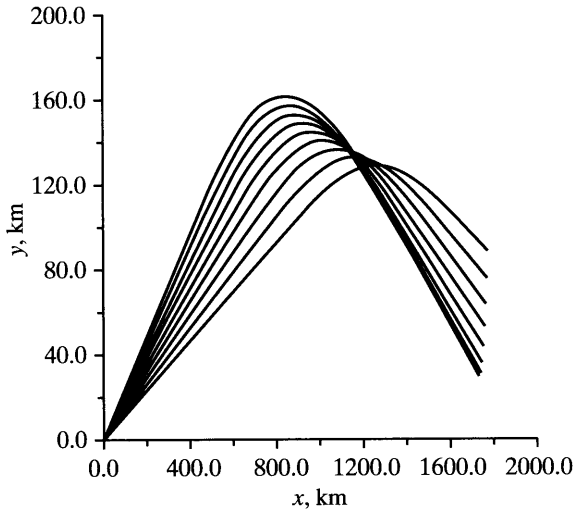

Fig. 35. Projections of space-time rays on the spatial coordinates for an instant frequency of f = 5.09 MHz and a longitudinal frequency modulation coefficient of Ω_x = 0.24 rad / (mks · km). The packet is focused at an altitude of y_m = 38 km

distribution (the beam altitude and width at distances of x = 300, 650, 1300, and 1700 km) obtained using the parabolic equation and shown in Fig. 19–22.

For example, the caustic effect corresponding to field compression (Fig. 21) is observed at a distance of x = 1300 km (Fig. 33).

In the previous section of this chapter, we synthesized two emitted signals focusing the field at altitudes of y_m = 22 km and y_m = 38 km. Figures 26–27 and 29–30 indicate that signals have rather complex functions of amplitude and frequency modulation.

To calculate rays using the modified STRO equations, we took the values of frequency and longitudinal frequency modulation for instants corresponding to the emitted signal peak power.

The projections of the space-time rays onto the (x, y) plane for the first (y_m = 22 km) and the second (y_m = 38 km) synthesized signals are given in Fig. 34 and 35, respectively.

In the first case, the frequency is $f = \omega/2\pi$ = 4.89 MHz, and the frequency modulation index is Ω_x = 0.21 rad/(mks · km).

In the second case, f = 5.09 MHz, and $\Omega_x \cdot$ = 0.24 rad/(mks · km).

The plots indicate that the space-time rays are focused at the corresponding altitudes, confirming the full-wave computations and that both methods can be used to adequately solve the stated problem.

§ 5. Discussion of results

In this chapter we show how we can artificially control ionospheric radio propagation using dispersive properties of a medium. Such a possibility is physically based on the dispersion refraction effect. Necessary transverse frequency modulation originates in the considered problem as a result of transformation of longitudinal modulation into transverse modulation in an inhomogeneous ionosphere.

The numerical computations, performed for the simplest model of the ionosphere, indicated that the usage of a special signal waveform makes it possible to considerably (by several orders of magnitude) increase the field energy at a chosen spatial point.

Such a signal should be subjected to frequency and amplitude modulation and occupy the band not narrower than 100 kHz.

Such broadband signals can be used, e.g., in communication systems with spread-spectrum signals (CDMA) as a single element of code sequence [92].

Along with an increase in energy characteristic, an additional advantage (related to the secrecy of communication) originates here: signal dispersive spreading is observed at all points (except the selected one) along the time coordinate, which additionally masks a signal against a background of noise.

Random fluctuations of plasma electron density, resulting in fluctuations of the wave phase front, are always present in the real ionosphere. This will result in a decrease in the effect of the spatial-temporal focusing, which was ignored when the above results were obtained. However, according to many experimental and theoretical works devoted to the effect of ionospheric fluctuations on spatial focusing of monochromatic waves (spatial caustics), this effect is insignificant at least in a quiet ionosphere. For example, the caustic zone is clearly defined and is almost always observed from the terminator line [55, 95, 100, 104, 105].

Since the scales of dispersion and ordinary refraction effects are commensurable, we can expect that random ionospheric inhomogeneities will insignificantly affect artificially created spatial-temporal focusing.